

# JGR Solid Earth

## RESEARCH ARTICLE

10.1029/2021JB023832

### Special Section:

Heterogeneity, anisotropy and scale-dependency: Keys to understand Earth composition, structure and behavior

### Key Points:

- We constrain the broadness of the iron spin crossover by a combination of novel experiments and computations
- We find a broad and asymmetric spin crossover range, which is sensitive to the distribution of iron in the ferropericlasite structure
- Ferropericlasite is in mixed-spin state throughout the lower mantle, but shows lateral spin state variations, impacting on mantle properties

### Supporting Information:

Supporting Information may be found in the online version of this article.

### Correspondence to:

A. S. J. Méndez and H. Marquardt,  
[alba.mendez@desy.de](mailto:alba.mendez@desy.de);  
[hauke.marquardt@earth.ox.ac.uk](mailto:hauke.marquardt@earth.ox.ac.uk)

### Citation:

Méndez, A. S. J., Stackhouse, S., Trautner, V., Wang, B., Satta, N., Kurnosov, A., et al. (2022). Broad elastic softening of (Mg,Fe)O ferropericlasite across the iron spin crossover and a mixed-spin lower mantle. *Journal of Geophysical Research: Solid Earth*, 127, e2021JB023832. <https://doi.org/10.1029/2021JB023832>

Received 14 DEC 2021

Accepted 9 AUG 2022

### Author Contributions:

**Conceptualization:** H. Marquardt

**Formal analysis:** A. S. J. Méndez, S. Stackhouse, V. Trautner, B. Wang, H. Marquardt

**Funding acquisition:** H.-P. Liermann, H. Marquardt

© 2022. The Authors.

This is an open access article under the terms of the [Creative Commons Attribution License](https://creativecommons.org/licenses/by/4.0/), which permits use, distribution and reproduction in any medium, provided the original work is properly cited.

## Broad Elastic Softening of (Mg,Fe)O Ferropericlasite Across the Iron Spin Crossover and a Mixed-Spin Lower Mantle

A. S. J. Méndez<sup>1,2</sup>, S. Stackhouse<sup>3</sup>, V. Trautner<sup>4</sup> , B. Wang<sup>4</sup> , N. Satta<sup>2,4</sup> , A. Kurnosov<sup>2</sup> , R. J. Husband<sup>1</sup> , K. Glazyrin<sup>1</sup> , H.-P. Liermann<sup>1</sup> , and H. Marquardt<sup>4</sup> 

<sup>1</sup>Deutsches Elektronen-Synchrotron DESY, Hamburg, Germany, <sup>2</sup>Bayerisches Geoinstitut BGI, University of Bayreuth, Bayreuth, Germany, <sup>3</sup>School of Earth and Environment, University of Leeds, Leeds, UK, <sup>4</sup>Department of Earth Sciences, University of Oxford, Oxford, UK

**Abstract** The elastic bulk modulus softening of (Mg,Fe)O ferropericlasite across the iron spin crossover induces dramatic changes in its physical properties, including seismic P-velocities and viscosity. Here, we performed compression of powders of (Mg<sub>0.8-0.9</sub>Fe<sub>0.2-0.1</sub>)O in a piezo-driven dynamic Diamond Anvil Cell (dDAC) and derive the bulk modulus by differentiation of pressure and volume data, providing first data on the broadness of the elastic softening for ferropericlasite with mantle-relevant compositions. We complement our experimental results with theoretical calculations that extend previous studies by considering multiple random configurations of iron, and going beyond treating high- and low-spin iron as an ideal solution. Both experiments and computations show a broad and asymmetric softening of the bulk modulus, and suggest that the softening is sensitive to the distribution of iron in the ferropericlasite structure. Our high-temperature calculations show that mixed-spin (Mg,Fe)O dominates the lower mantle at all depths below 1,000 km. In contrast to most previous works, we find that ferropericlasite will not exist in pure low-spin state along a typical mantle geotherm. Based on our model, the physical properties of ferropericlasite will show significant lateral variation at depths below 1,400 km, with the strongest effects expected between 2,000 and 2,600 km.

**Plain Language Summary** Understanding the physical properties of deep mantle minerals is pivotal to interpret geophysical observables and constrain large-scale geodynamic models. (Mg,Fe)O ferropericlasite is the second most abundant mineral in Earth's lower mantle, ranging from 660 to 2,890 km depths. Previous works have shown that the electronic configuration of iron in ferropericlasite changes at pressures corresponding to the mid-mantle. This process, called iron-spin crossover, markedly affects a variety of physical properties, including seismic wave speeds and viscosity. Here we combine novel experiments and theoretical calculations to provide a coherent picture of the onset depth and broadness of the spin crossover in Earth's lower mantle. We show that the spin crossover happens throughout most of the lower mantle, altering physical properties at most depths up to the core-mantle boundary. This quantitative understanding is key to model the impacts of the spin crossover on geophysical mantle properties and mantle dynamics.

## 1. Introduction

(Mg,Fe)O ferropericlasite is the second most abundant mineral in Earth's lower mantle (e.g., Irifune et al., 2015). At room pressure, ferrous iron (Fe<sup>2+</sup>) in ferropericlasite adopts the high-spin electronic configuration where the six 3d-electrons partially fill the  $t_{2g}$  and  $e_g$  orbitals, maximizing the number of unpaired electrons. At a pressure of about 40 GPa, a distortion of the iron-containing octahedral sites in the crystal structure triggers a change in iron electronic configuration to the low-spin state, where electron pairing in the  $t_{2g}$  orbitals is favored (Badro et al., 2003). Several studies have shown that the properties of ferropericlasite in mixed-spin state are markedly different from those in either high- or low-spin state. In particular, the spin crossover is accompanied by a reduction in the Fe<sup>2+</sup> ionic radius (Shannon, 1976) enhancing the compressibility of ferropericlasite over the pressure range where the spin crossover occurs (Crowhurst et al., 2008; Lin et al., 2013). This enhanced compressibility of ferropericlasite in mixed-spin state causes a significant decrease in seismic P-wave velocities (Crowhurst et al., 2008; Marquardt et al., 2009; Wentzcovitch et al., 2009; Yang et al., 2015) with implications for the interpretation of seismic observables (Cammarano et al., 2010; Kennett, 2021; Shephard et al., 2021), and might lead to a marked decrease in viscosity (Deng & Lee, 2017; Marquardt & Miyagi, 2015; Saha et al., 2013; Wentzcovitch et al., 2009). Quantifying the presence and distribution of mixed-spin state ferropericlasite in the lower mantle, including its lateral variations, is thus pivotal to interpret seismic observables and design geodynamic models.

**Investigation:** A. S. J. Méndez, S. Stackhouse, N. Satta, A. Kurnosov, K. Glazyrin, H. Marquardt  
**Methodology:** A. S. J. Méndez, S. Stackhouse, R. J. Husband, H.-P. Liermann, H. Marquardt  
**Project Administration:** H.-P. Liermann, H. Marquardt  
**Software:** V. Trautner, B. Wang, R. J. Husband  
**Supervision:** H.-P. Liermann, H. Marquardt  
**Visualization:** S. Stackhouse, V. Trautner, H. Marquardt  
**Writing – original draft:** S. Stackhouse, H. Marquardt  
**Writing – review & editing:** A. S. J. Méndez, S. Stackhouse, V. Trautner, R. J. Husband, K. Glazyrin, H.-P. Liermann, H. Marquardt

Recent attempts to detect an expression of the iron spin crossover in tomographic models derived from seismic observations (Shephard et al., 2021) relied on theoretical calculations to predict the spin crossover at mantle temperatures. The employed calculations, however, were based on models where the distances between iron atoms were maximized, and assumed ideal mixing of high- and low-spin iron (Wu et al., 2013), similar to other studies (Muir & Brodholt, 2015; Tsuchiya et al., 2006; Wentzcovitch et al., 2009; Wu & Wentzcovitch, 2014), which produce a sharp crossover at 300 K. In contrast, previous experimental work showed that at ambient pressure ferroprecipitate samples quenched from high temperature (~1000 K) largely exhibit random ordering (Waychunas et al., 1994), suggesting that maximizing the distance between iron atoms might not well describe natural systems. Furthermore, recent calculations showed that there is a favorable enthalpy of mixing of high- and low-spin iron (Holmström & Stixrude, 2015), which leads to a substantial broadening of the spin crossover and hence bulk modulus softening and geophysical signature in the mantle.

Diamond Anvil Cell (DAC) experiments can provide direct constraints on the bulk modulus of (Mg,Fe)O across the spin crossover that can be used to benchmark theoretical predictions. Existing experimental works reported a substantial elastic softening (Crowhurst et al., 2008; Marquardt et al., 2018; Yang et al., 2015), but the pressure range over which the decrease of the bulk modulus is observed varies. Early measurements on (Mg<sub>0.94</sub>Fe<sub>0.06</sub>)O using Impulsive Stimulated Light Scattering (ISLS) reported a bulk modulus softening between 40 and 60 GPa (Crowhurst et al., 2008), whereas more recent work on (Mg<sub>0.92</sub>Fe<sub>0.08</sub>)O using the same technique observed the softening up to a pressure of almost 80 GPa (Yang et al., 2015). Pressure oscillation experiments in the dynamic DAC in combination with time-resolved X-ray diffraction diagnostics reported a similarly broad crossover range extending from about 40 to 80 GPa (Marquardt et al., 2018). The latter is the only study to directly measure the bulk modulus softening for iron contents above 8 at.%, but has a limited pressure coverage within the spin crossover region and was performed in non-hydrostatic conditions without a pressure-transmitting medium.

Modeling of the bulk modulus based on traditional X-ray diffraction data generally predicts a sharper softening across the spin crossover (Lin et al., 2013; Mao et al., 2011; Marquardt et al., 2009). However, the sharpness of the resulting bulk modulus softening depends on model assumptions and is poorly constrained by the actual data that typically cover only a few pressure points across the spin change (Fei et al., 2007a, 2007b; Lin et al., 2005; Marquardt et al., 2009; Solomatova et al., 2016).

Here we used a dynamic Diamond Anvil Cell (dDAC) driven by a piezoelectric actuator (Evans et al., 2007; Jenei et al., 2019) to compress ferroprecipitate powders across the spin crossover using neon as pressure-transmitting medium. We employed extremely sensitive X-ray detectors in combination with the dDAC to perform time-resolved X-ray diffraction measurements along the compression path. The excellent pressure resolution of our data, about 0.1–0.5 GPa, together with the smooth compression path achieved by the dDAC, enables us to directly quantify the bulk modulus of ferroprecipitate across the spin crossover, without the need for model assumptions (Méndez et al., 2021). To complement our experiments, we performed first-principles calculations, where we considered multiple random distributions of iron and did not treat high- and low-spin iron as an ideal solution. Both our experimental and computational data show a broad asymmetric spin crossover region. We use our high-temperature calculations to predict the low-spin fraction in the lower mantle, and find the spin crossover to cover a wider pressure-temperature space than predicted by previous works used for comparison to seismic tomography models (Shephard et al., 2021).

## 2. Materials and Methods

### 2.1. Experimental Details

#### 2.1.1. High-Pressure Dynamic Diamond-Anvil Cell Experiments

Powders of (Mg<sub>0.8</sub>Fe<sub>0.2</sub>)O and (Mg<sub>0.9</sub>Fe<sub>0.1</sub>)O were synthesized from stoichiometric mixtures of reagent grade MgO and Fe<sub>2</sub>O<sub>3</sub> treated in a gas-mixing furnace at 1,250°C at an oxygen fugacity of 2 log units below the fayalite-magnetite-oxygen (FMQ) buffer (see also Marquardt & Miyagi, 2015). Fine-grained platinum powder was mixed with the sample and used as a pressure marker. Rhenium gaskets were preindented to a thickness of about 30 μm in a symmetric DAC with 200 μm anvil culets and holes with 150 μm diameters were drilled in the gaskets. Given the typically small amount of sample required for gas loading in DACs and the relatively low Z-character of (Mg,Fe)O in comparison to Re, an amorphous Fe<sub>0.79</sub>Si<sub>0.07</sub>B<sub>0.14</sub> insert was placed in the Re gasket hole in order to avoid emergence of Re peaks in the diffraction patterns of (Mg<sub>0.8</sub>Fe<sub>0.2</sub>)O (Méndez et al., 2020),

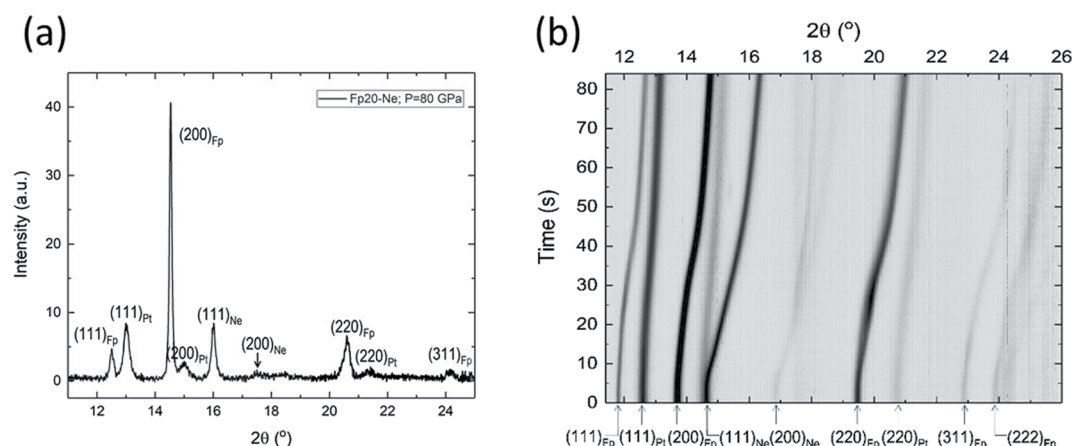


**Figure 1.** (a) A typical integrated diffraction pattern collected in 200 ms from  $(\text{Mg}_{0.8}\text{Fe}_{0.2})\text{O}$  in neon at 80 GPa. (b) Contour plot showing the experimental run on  $(\text{Mg}_{0.8}\text{Fe}_{0.2})\text{O}$ , where 337 individual diffraction images have been collected upon compression.

Figure 1a. The  $(\text{Mg},\text{Fe})\text{O}$ -Pt mixture was loaded into the gasket hole and neon was loaded as pressure-transmitting medium using the gas-loading setup at the Extreme Conditions Beamline (ECB) at PETRA III, DESY, Germany (Liermann et al., 2015). Samples were precompressed by uniformly tightening the screws as in standard DAC experiments. The DACs were inserted in a “cap housing” coupled to a high voltage piezoelectric (PE) actuator (Jenei et al., 2019). DAC and PE were engaged by tightening the cap at the back of the housing. When a given voltage is applied, the PE expands and pushes against the DAC in the housing compressing the sample. Trapezoidal voltage-time waveforms were generated using the program *Benchlink Waveform Builder* (Keysight Technologies) and loaded on a waveform generator (Agilent 33522B). A delay generator (SRS, DG645/5 with Rb clock) and a piezo amplifier (Piezosystem Jena GmbH) are employed when sending the waveform to the PE (Jenei et al., 2019).

Intense monochromatic synchrotron X-ray radiation (0.48 Å wavelength) was used for time-resolved X-ray diffraction measurements at the ECB (Liermann et al., 2015), focused using a compound refractive lens (2 (h)  $\mu\text{m}$   $\times$  8 (v)  $\mu\text{m}$ , FWHM). X-ray diffraction images were collected on a GaAs 2.3 MPix LAMBDA detector that allows for data collection at a repetition rate of up to 2 kHz (Pennicard et al., 2013, 2018). The detector was placed with an offset to the sample center, capturing sections of the Debye–Scherrer diffraction rings. Tilting and rotation of the detector and sample-detector distance were calibrated using a  $\text{Cr}_2\text{O}_3$  standard (NIST 674b). Data analysis software developed at the ECB was used for quick visualization of the collected data in contour plots (Figure 1b). Diffraction images were integrated using the program Dioplas (Prescher & Prakapenka, 2015). The integrated and background corrected diffraction patterns were processed using a customized python code for batch processing to extract the peak positions of the sample and platinum.

Data collection on  $(\text{Mg}_{0.8}\text{Fe}_{0.2})\text{O}$  was done continuously during a single continuous compression ramp from about 33 to 97 GPa with compression rates of 0.3–1.2 GPa/s (Figure S5 in Supporting Information S1), equating to volumetric strain rates in  $(\text{Mg},\text{Fe})\text{O}$  of about  $2\text{--}5 \cdot 10^{-3} \text{ s}^{-1}$ . Single image exposure time was 200 ms, leading to a total of 337 XRD images collected during compression. The unit cell volume of the sample was determined by fitting the (111), (200), and (220) diffraction lines of ferropericlase  $\text{Fp}_{(111)}$ ,  $\text{Fp}_{(200)}$ ,  $\text{Fp}_{(220)}$ . Pressure was determined from the measured position of the (111) diffraction line of platinum,  $\text{Pt}_{(111)}$ , using published equation of state parameters (Fei et al., 2007a). Additional data on  $(\text{Mg}_{0.9}\text{Fe}_{0.1})\text{O}$  were collected with single image exposure time of 400 ms in three compression steps, ranging from 30 to 48 GPa, 47 to 69 GPa, and 70 to 84 GPa (total of 771 XRD images). Results for  $(\text{Mg}_{0.9}\text{Fe}_{0.1})\text{O}$  are shown in the Supplementary Material.

### 2.1.2. Derivation of High-Pressure Bulk Moduli

The dense pressure-coverage in our data allows for a direct determination of the bulk modulus according to its thermodynamic definition ( $K_T = -V \cdot (\partial P / \partial V)_T$ ). We calculated the bulk modulus from the slope of a linear fit to  $V(P)$  applied over different pressure intervals (Figure S1 in Supporting Information S1). As expected, a larger chosen pressure interval leads to smaller nominal uncertainties as derived from the standard error of the linear

fit to the  $V(P)$  data. However, this comes at the expense of a reduced effective pressure resolution. We decided to use a pressure interval of 2.5 GPa (i.e.,  $\pm 1.25$  GPa around target pressure), typically containing about 10–20 measured  $V(P)$  points. We found this interval to represent the best compromise between pressure resolution and uncertainties in derived bulk moduli (Figure S2 in Supporting Information S1). The uncertainties in calculated bulk moduli are smallest if they are derived from the unit cell volume calculated from the (200) line of ferroperricite only, instead of using the average volume in the derivation. By using the strongest diffraction line, volume scatter is minimized, leading to the smoothest pressure derivatives. The bulk moduli reported in Figure 3 and used for comparison to the computational results are thus based on the (200) line only. We note, however, that the choice of the ferroperricite diffraction line does not substantially affect  $K(P)$  or its trend, see comparison to results based on the average volumes in Figure S3 in Supporting Information S1.

## 2.2. Calculation Details

### 2.2.1. Model Systems

To enable direct comparison with the experimental results, models of ferroperricite were constructed with the chemical compositions  $(\text{Mg}_{0.8125}\text{Fe}_{0.1875})\text{O}$  and  $(\text{Mg}_{0.90625}\text{Fe}_{0.09375})\text{O}$ , corresponding to 6 or 3 Fe atoms in a 64 atom cell. For simplicity, we will refer to the two modeled compositions as  $(\text{Mg}_{0.8}\text{Fe}_{0.2})\text{O}$  and  $(\text{Mg}_{0.9}\text{Fe}_{0.1})\text{O}$  throughout the discussion. In order to investigate the possible role of short-range order on spin crossover pressure (Glazyrin et al., 2017; Kantor et al., 2009), 20 models were constructed for each ferroperricite composition, with different random arrangements of Fe. For comparison, we also created a high symmetry model with a  $(\text{Mg}_{0.8125}\text{Fe}_{0.1875})\text{O}$  composition. The initial atomic coordinates of the Fe in these models are listed in Table S1 in Supporting Information S1 and depicted in Tables S2–S3 in Supporting Information S1.

In the 64-atom models, neighboring on-axis iron atoms correspond to infinite rows of atoms with an Fe–O–Fe–O sequence. In order to assess the impact of this on the results, larger 216-atom models were constructed (see Tables S4–S7 in Supporting Information S1). These contained the same number and arrangement of iron atoms as the 64-atom models, but their larger size ensured that there were no iron arrangements corresponding to infinite rows of atoms with an Fe–O–Fe–O sequence.

### 2.2.2. First-Principles Calculations

Theoretical calculations were performed with VASP (Kresse & Furthmüller, 1996a, 1996b), employing the projector augmented wave method (Blöchl, 1994; Kresse & Joubert, 1999), within the framework of density functional theory (DFT). The LDA exchange-correlation functional was used (Perdew & Zunger, 1981). The valence electron configurations for the potentials were  $2p^63s^2$  for Mg,  $3p^63d^74s^1$  for Fe, and  $2s^22p^4$  for O. The kinetic-energy cut-off for the plane-wave basis set was set to 600 eV. For the 64-atom models, the Brillouin zone was sampled using a  $2 \times 2 \times 2$  Monkhorst-Pack grid (Monkhorst & Pack, 1976), while for the larger 216-atom models it was restricted to the gamma-point. The break condition for the electronic self-consistent loop was  $10^{-6}$  eV and that for ionic relaxation was  $10^{-5}$  eV. These parameters ensured that calculated enthalpy differences were converged to less than 1 meV per atom and bulk moduli to within 1 GPa. Symmetry was switched off.

In order to accurately describe the strongly correlated  $d$  electrons of iron in ferroperricite, we utilized the LDA + U method (Anisimov et al., 1991, 1997), in particular, the scheme of Dudarev et al. (1998) in which only the difference between onsite Coulomb interaction parameter  $U$  and onsite exchange parameter  $J$  is meaningful. In the present work,  $U - J = 3.3$  eV was found to give the best agreement with experimental values for the spin crossover pressure. This value is similar to the  $U - J = 3.0$  eV used in previous calculations of ferroperricite (Muir & Brodholt, 2015).

The pressure and temperature dependence of the spin crossover was calculated following a similar approach to that of previous studies (Tsuchiya et al., 2006; Wentzcovitch et al., 2009). However, in contrast to these studies and following the observations of Holmström and Stixrude (2015), we did not assume an ideal solution for high- and low-spin iron when calculating enthalpy differences, instead calculating the enthalpy of mixed-spin states, as well as high- and low-spin.

Since the LDA is known to underestimate pressure, we calculated a correction using the method outlined by Oganov et al. (2001), but excluding the thermal pressure term, which is expected to be small. The correction was calculated to be +6 GPa, based on the ambient condition volume of  $76.1 \text{ Å}^3$  reported by Speziale et al. (2007).

### 2.2.3. Magnetic Ordering

For the iron concentrations investigated in this study, ferropericlase is paramagnetic at 300 K (Kantor et al., 2009; Lyubutin et al., 2013; Speziale et al., 2005). It is difficult to model paramagnetic systems and so in our theoretical calculations, the initial high-spin states were modeled both as ferromagnetic and antiferromagnetic and the results of both sets of calculations were averaged. For the antiferromagnetic calculations, initial magnetic moments were assigned in such a manner that iron atoms close to one another were given opposite spins.

In order to investigate the influence of magnetic state we calculated the spin crossover pressure for Models 7 and *symm* with a (Mg<sub>0.8125</sub>Fe<sub>0.1875</sub>)O composition, for over 30 different magnetic orderings, representing disordered collinear paramagnets (Figure S7 in Supporting Information S1). The spin crossover pressures are defined as going from the full high-spin state to full low-spin state. Model 7 has a random arrangement of iron atoms, with only off-axis neighbors. For this model the spin crossover pressures only varied by about 3 GPa. Model *symm* has an ordered arrangement of iron atoms, with only on-axis neighbors. For this model the spin crossover pressure varied by about 10 GPa, from about 46 GPa for ferromagnetic ordering, to close to 56 GPa for the highest symmetry antiferromagnetic ordering, with pressures for other orderings inbetween. This suggests that magnetic ordering is primarily important for models with a high number of neighboring on-axis iron atoms.

### 2.2.4. Spin Crossover

The pressure and temperature dependence of the spin crossover was calculated following a similar approach to that of previous studies (Tsuchiya et al., 2006; Wentzcovitch et al., 2009), where the fraction of low-spin iron is calculated from the expression:

$$n(P, T) = \frac{1}{1 + m(2S + 1)\exp\left[\frac{\Delta H_{LS-HS}(P, T)}{k_B X_{Fe} T}\right]} \quad (1)$$

Here  $m$  is the electronic configuration degeneracy ( $m = 3$  for high-spin and  $m = 1$  for low-spin),  $S$  is the spin quantum number ( $S = 2$  for high-spin and  $S = 0$  for low-spin),  $\Delta H_{LS-HS}$  is the difference in the enthalpy of the high- and low-spin states,  $k_B$  is the Boltzmann constant,  $X_{Fe}$  is the fraction of iron and  $T$  is temperature. However, in contrast to these studies and following the observations of Holmström and Stixrude (2015), we did not assume an ideal solution for high- and low-spin iron when calculating  $n(P, T)$ , but calculate the enthalpy of mixed-spin states, as well as high- and low-spin. For each model studied, we calculated the enthalpy difference between all stable spin-states, including stable mixed-spin states, as a function of pressure (e.g., Figure S8a in Supporting Information S1) and used Equation 1 to determine  $n(P, T)$  for each spin crossover (e.g., Figure S8b in Supporting Information S1). In this procedure,  $\Delta H_{LS-HS}$  is the enthalpy difference between a lower and higher spin state and  $X_{Fe}$  the fraction of iron in the model weighted by the fraction of iron involved in the individual spin crossover, i.e. for a model with (Mg<sub>(1-x)</sub>Fe<sub>x</sub>)O composition and a spin crossover where  $a$  out of  $b$  iron atoms go to low-spin:  $X_{Fe} = (a/b) \times x$ . The  $n$  value for a model is then the weighted average of the  $n$  values for the series of spin crossovers between high- and low-spin states, where the weights are their  $(a/b)$  values, for example, Figure S8b in Supporting Information S1. The  $n$  value for a particular ferropericlase composition was calculated as the arithmetic mean of the  $n$  values of all models with that composition, including both magnetic states. To allow direct comparison with the 64-atoms models, for the calculation of  $n$  using the 216-atom models,  $x$  was assumed to be the same value as that for the corresponding 64-atom model.

To reduce the number of calculations, this was achieved by first calculating the enthalpy of all spin states with one low-spin iron. Once the most favorable spin state with one low-spin iron was identified, it was used as the basis for constructing spin states with two low-spin irons. Once the most favorable spin state with two low-spin irons was identified, it was used as the basis for constructing spin states with three low-spin irons and so on and so forth. Enthalpy differences were calculated for each spin state at 20 GPa, 40 GPa, 60 GPa and 80 GPa. For the (Mg<sub>0.8125</sub>Fe<sub>0.1875</sub>)O composition, it was not always possible to stabilize a high-spin antiferromagnetic state at 80 GPa and a calculation was carried out at a lower pressure of 50 GPa instead. For one iron configuration (Model 1 of the (Mg<sub>0.8125</sub>Fe<sub>0.1875</sub>)O composition) the results of this procedure were compared with those obtained when calculating all possible mixed-spin states, and were found to be identical.



Note that, as in previous studies (Tsuchiya et al., 2006) we neglect the vibrational free energy in the calculation of  $n(P, T)$ . Previous calculations (Wentzcovitch et al., 2009) have shown that this is important at lower mantle temperatures, but has a minor effect at room temperature.

### 2.2.5. Equation of State

To determine the volume of ferroperricite through the spin crossover, the volume of mixing of the pure low- and high-spin states was assumed to be ideal

$$V(n) = (1 - n)V_{HS}(P) + nV_{LS}(P) \quad (2)$$

where  $V(n)$  is the volume of ferroperricite with a low-spin fraction  $n$ , and  $V_{HS}$  and  $V_{LS}$  are the volumes of ferroperricite in the pure high- and low-spin states. Our calculations for the  $(\text{Mg}_{0.8125}\text{Fe}_{0.1875})\text{O}$  composition, showed that the maximum deviation of the volume of a mixed-spin state from that predicted from ideal mixing of the volumes of the pure high- and low-spin states was on the order of 0.2%, with an average deviation of 0.05%. The latter equates to a volume of about  $0.05\text{\AA}^3$  per unit cell for the largest volume, and less for others.

For each ferroperricite composition, the volume difference between different models in the same spin-state (i.e., the same number of high- and low-spin iron) was on the order of 0.2%. In view of this, for simplicity, an equation of state was only calculated for one model for each ferroperricite composition. For the  $(\text{Mg}_{0.90625}\text{Fe}_{0.09375})\text{O}$  composition, this was Model 1, while for the  $(\text{Mg}_{0.8125}\text{Fe}_{0.1875})\text{O}$  composition, this was Model *symm*. The volumes of these models were calculated for the pure high- and low-spin states at 13 pressures between  $-10$  and  $140$  GPa. The resulting pressure-volume curves were fit to a third-order Birch-Murnaghan equation-of-state (Birch, 1947; Murnaghan, 1944), which were used to compute the volume of the pure high- and low-spin states ( $V_{HS}$ ,  $V_{LS}$ ) and corresponding bulk moduli ( $K_{HS}$ ,  $K_{LS}$ ), required for Equations 2 and 3. The same values were used for calculating  $V(n)$  and  $K(n)$ , when using  $n$  values from both 64-atom and 216-atom models.

All calculations were static and neglect thermal pressure. The effect of neglecting thermal pressure on the equation of state is expected to be small at 300 K and is, in part, accounted for through the ad hoc pressure correction, described above. These arguments follow through to the calculation of the bulk modulus below, which are based on these equations of state.

### 2.2.6. Bulk Modulus

Following previous theoretical studies (Tsuchiya et al., 2006; Wentzcovitch et al., 2009), the bulk modulus across the spin crossover was calculated from the relation

$$\frac{V(n)}{K(n)} + (1 - n)\frac{V_{HS}}{K_{HS}} + n\frac{V_{LS}}{K_{LS}} - (V_{LS} - V_{HS})\left(\frac{\partial n}{\partial P}\right)_T \quad (3)$$

where all terms are as defined above and the pressure derivative of the fraction of low-spin iron was calculated at 300 K from a centered finite-difference approximation.

Note that, although  $n$  is calculated at 300 K,  $V(n)$ ,  $V_{HS}$ ,  $V_{LS}$ ,  $K_{HS}$  and  $K_{LS}$  are all static values, which will influence  $K(n)$ . As already mentioned above, we expect the difference between our static values and 300 K values to be small. In addition, we also note that previous calculations (Tsuchiya et al., 2006; Wentzcovitch et al., 2009) indicate that the temperature derivatives of the bulk modulus of the pure high- and low-spin states of ferroperricite are on the order of 0.02 GPa/K. These derivatives imply that, without a pressure correction, static values for the bulk moduli will be about 6 GPa higher than 300 K values, which is smaller than the errors associated with the experimental measurements.

Our theoretical results provide atomic scale understanding of how the arrangement of iron influences the spin crossover. In Tables S2 and S3 in Supporting Information S1 we report the structures, low-spin fraction at 300 K and Fe-Fe radial distribution function for all 64-atom models studied. Fe-Fe radial distribution functions were calculated using VMD (Humphrey et al., 1996). In Tables S4-S7 in Supporting Information S1 we report the structures and compare the low-spin fraction at 300 K for 64-atom and 216-atom models. Labels indicate the order that the iron atoms undergo a spin crossover. Together these show that the pressure at which individual iron atoms undergo a spin crossover depends on several factors: the number and type (on or off-axis) of neighboring iron atoms, whether the neighboring iron atoms are in a high- or low-spin state and to a certain extent whether they have the same or opposite spin (Tables S2-S7 in Supporting Information S1).

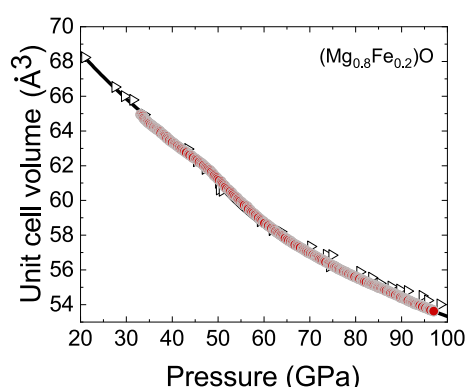


**Figure 2.** Unit cell volumes derived as weighted average of (111), (200), and (220) lines from  $(\text{Mg}_{0.8}\text{Fe}_{0.2})\text{O}$  measured in experiments using neon as pressure-transmitting medium. A total of 337 XRD images were collected during compression. The uncertainty in experimental volumes is smaller than the symbol size. Complementary computational results are shown as solid curve. Previously published X-ray diffraction data on  $(\text{Mg}_{0.83}\text{Fe}_{0.17})\text{O}$  (Lin et al., 2005) are shown as open black triangles for comparison.

### 3. Results and Discussion

The experimental and computational unit cell volumes for  $(\text{Mg}_{0.8}\text{Fe}_{0.2})\text{O}$  and  $(\text{Mg}_{0.9}\text{Fe}_{0.1})\text{O}$  are plotted as a function of pressure in Figures 2 and S6 in Supporting Information S1. There is good agreement between XRD data measured earlier for  $(\text{Mg}_{0.83}\text{Fe}_{0.17})\text{O}$  and  $(\text{Mg}_{0.9}\text{Fe}_{0.1})\text{O}$  in static DAC experiments (Lin et al., 2005; Marquardt et al., 2009). The agreement of the here-measured volumes with previous experimental data collected in static DAC experiments suggests that our compression rate is sufficiently slow for the system to not suffer from non-equilibrium effects that may be encountered in dynamic compression experiments, at least not more than possibly present in traditional static DAC experiments where measurements are taken on the time-scale of minutes (Glazyrin et al., 2020). We note that the use of neon as pressure-transmitting medium unavoidably leads to deviatoric stress in our experiments at high pressure (Dorfman et al., 2012; Meng et al., 1993). Stress levels at the here-employed compression rates, however, are expected to be comparable to previous experiments in neon carried out under static compression, see Figure S4 in Supporting Information S1. A stress analysis based on the line-shift of the (111) and (200) lines of Pt suggests about 2 GPa of differential stress in our experiments, comparable to that expected in static DAC compression experiments in neon (Dorfman et al., 2012), Figure S5 in

Supporting Information S1. Temperature annealing might help to reduce differential stresses (Meng et al., 1993), but is not compatible with the continuous compression carried out here.

Our unit cell volume data for ferropericlase show a significant volume drop at a pressure of around 40 GPa indicating the onset of the iron spin crossover. The change of trend in  $V(P)$  becomes very clear in our data due to the quasi-continuous pressure coverage. We derive the bulk modulus directly from our data without any smoothing or the need to assume its behavior across the spin crossover as required in previous works (Lin et al., 2005; Marquardt et al., 2009; Solomatova et al., 2016). The bulk moduli are plotted as a function of pressure in Figures 3 and S6 in Supporting Information S1, together with the here-performed ab-initio calculations. Both measured and calculated bulk moduli for  $(\text{Mg}_{0.8}\text{Fe}_{0.2})\text{O}$  and  $(\text{Mg}_{0.9}\text{Fe}_{0.1})\text{O}$  show a clear drop at a pressure of about 40–45 GPa associated with the spin crossover, where the onset pressure slightly shifts to higher pressures with iron content. Overall, our data show a broad and asymmetric shape of the softening for  $(\text{Mg}_{0.8}\text{Fe}_{0.2})\text{O}$ , and to a lesser extent for  $(\text{Mg}_{0.9}\text{Fe}_{0.1})\text{O}$ . Little difference is seen between the results of the 64-atom and the 216-atoms models.

Overall our findings suggest that the bulk modulus is lowered over a wide pressure range for  $(\text{Mg}_{0.8}\text{Fe}_{0.2})\text{O}$ . Previous calculations predicted a sharp bulk modulus softening at room temperature and do not reproduce our experimental results well (Wentzcovitch et al., 2009). In assuming an ideal solution for high- and low-spin iron, all iron atoms undergo the spin crossover at the same pressure at 0 K, causing a very sharp bulk modulus softening (Wentzcovitch et al., 2009). Our broader bulk modulus softening, and hence wider spin crossover range at 300 K, appears to be supportive of the work of Holmström and Stixrude (2015), who attribute the observed broadness of the spin crossover at low temperatures (300 K) to the favorable enthalpy of mixing  $\Delta H_{\text{mix}}$ . The magnitude of the enthalpy of mixing, however, is affected by the arrangement of Fe atoms, as predicted by Holmström and Stixrude (2015), who studied a highly symmetric arrangement of iron with periodic Fe-O-Fe-O sequences. Our computations for  $(\text{Mg}_{0.8}\text{Fe}_{0.2})\text{O}$ , that account for a random distribution of iron, predict a mixed-spin state for a pressure interval of about 40 GPa at room temperature. Our results are thus intermediate between the previous computational works, where Wentzcovitch et al. (2009) suggest a crossover range of only about 10 GPa, and Holmström and Stixrude (2015) predicted the range to span about 80 GPa.

Our results not only show a broad spin crossover region, but also point toward a multi-dip structure where (at least) two local minima are noticeable in the experimental data as well as the theoretical calculations (Figure 3). Our calculations indicate that the origin of these anomalies are iron atoms in different local environments undergoing spin crossovers at different pressures (Tables S2–S7 in Supporting Information S1). Most iron atoms undergo a spin crossover at about 40–50 GPa, leading to the large first anomaly. The other anomalies correspond primarily to iron atoms that have neighboring on-axis iron atoms in the low-spin state. For such iron atoms, the favorable enthalpy of mixing of high- and low-spin states stabilizes the high-spin iron atoms to higher pressures. Our

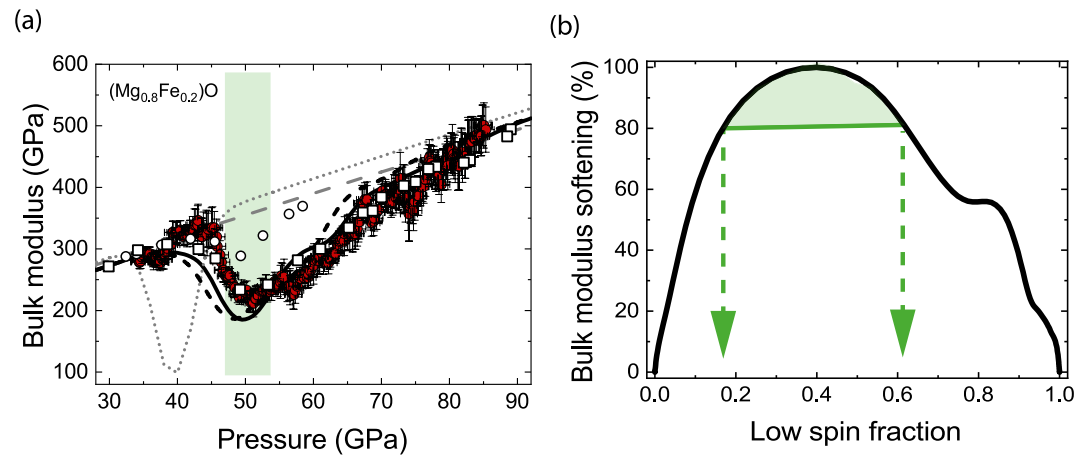


**Figure 3.** (a) Bulk moduli derived by direct differentiation of our experimentally measured  $V(P)$ -data in comparison to our ab-initio calculations, using multiple models with random configurations of iron, which represent different local iron environments. Computational results are shown as solid black curves (64 atoms model) and dashed black curves (216 atoms model). Previous computational work on  $(\text{Mg}_{0.8175}\text{Fe}_{0.1825})\text{O}$  (Wentzcovitch et al., 2009), using a model where iron atoms are far apart and presuming ideal mixing of high- and low-spin irons, are shown as dotted curve. Experimental results for  $(\text{Mg}_{0.94}\text{Fe}_{0.06})\text{O}$  (open circles) and  $(\text{Mg}_{0.92}\text{Fe}_{0.08})\text{O}$  (open squares) derived from optical spectroscopy measurements (Crowhurst et al., 2008; Yang et al., 2015) are shown for comparison. The dashed gray line shows the bulk modulus predicted for  $\text{MgO}$  by computations (Karki et al., 1999). The green shaded region refers to the range of pressure where the bulk modulus softening reaches >80% of its maximum value (see (b)). (b) Bulk modulus softening (in %), where 100% refers to the maximum softening that occurs relative to a simple average of pure high- and low-spin bulk moduli. The green arrows indicate the low-spin fractions between which 80% of the maximum softening occurs.

calculations show that as the spin crossover nears completion, it is the iron atoms with the most low-spin neighboring iron atoms that persist in the high-spin state to the highest pressures, in particular, those that have low-spin on-axis neighboring iron atoms. Our results thus suggest that the effect of the favorable enthalpy of mixing is most significant for on-axis neighboring iron atoms pairs, which makes sense given that it is the on-axis  $d$ -orbitals ( $dz^2$  and  $dx^2-y^2$ ) that become unoccupied when iron atoms undergo a spin crossover. In a similar manner we find that in our calculations, when present, iron atoms with a high-spin on-axis neighbor are often the first to undergo a spin crossover.

The agreement between our computations and the here-reported experimental results suggest that (a) the mixed-spin region cannot be modeled assuming ideal mixing of high- and low-spin iron, (b) the shape of the  $K(P)$  curve, and low-spin fraction, is sensitive to the distribution of iron in the ferropiclasite lattice, and (c) the assumption of a random distribution of iron atoms in the ferropiclasite structure is broadly valid. The slight disagreement observed between the here-reported experimental and computational results might be related to deviations from a random distribution in the experimental samples and/or the effect of deviatoric stress in the sample.

Extension of our theoretical model, which is in good agreement with our experiments, to high temperatures allows us to pinpoint the expected onset depth and broadness of the spin crossover in different regions of the lower mantle (Figure 4). In Figure 4b, we show the here-derived low-spin fractions of ferropiclasite along a typical lower mantle geotherm as well as their changes with expected temperature variations in the lower mantle. Expected depth-dependent mantle temperature variations were taken from a geodynamic model (Figure 3c in Davies et al., 2012). Here, we are particularly interested in constraining the depth regions in the mantle, where the most significant alterations of ferropiclasite properties by the spin crossover are expected. For the following discussion, and based on the bulk modulus softening observed in our room temperature results, we assume that the largest impact occurs when the low-spin fraction is between 0.18 and 0.62 (shown as green shaded region in Figure 4b). For this range of low-spin fractions, the bulk modulus reduction of ferropiclasite reaches >80% of its maximum value (see Figure 3b). Figure 4b shows that, while the onset depth of the spin crossover is about 1,000 km, it will start to markedly affect properties below ~1,400 km. The onset depth only mildly changes within the range of expected temperature variations, and hence with geographic location in the mantle. In stark contrast to the weak effect on onset depth, temperature variations in the mantle have a marked influence on the



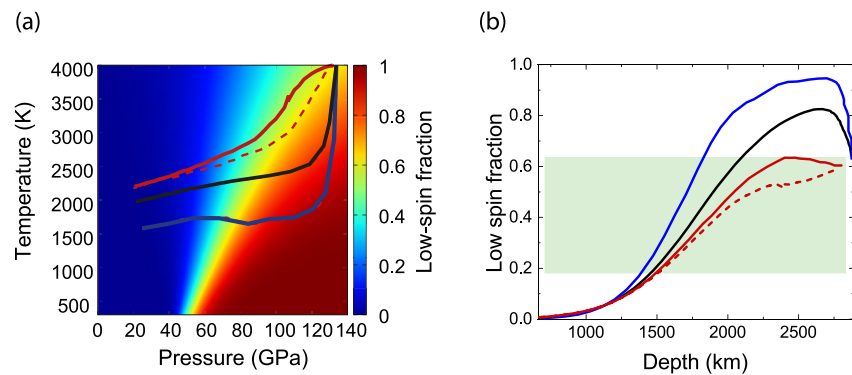


**Figure 4.** Low-spin fraction of  $(\text{Mg}_{0.8175}\text{Fe}_{0.1825})\text{O}$  in Earth's lower mantle. (a) Spin fractions as function of pressure and temperature for model-1. A typical lower mantle geotherm is shown as a black curve, along with lateral temperature variations in the mantle, where expected temperature variations are taken from a previous modeling (Davies et al., 2012). Blue: Cold regions of the lower mantle, red: Hot regions of the lower mantle, where the difference between the solid and dashed curves relates to a purely thermal or thermo-chemical model, respectively (details in Davies et al. (2012)). (b) Low-spin fraction of iron in  $(\text{Mg}_{0.8175}\text{Fe}_{0.1825})\text{O}$  expected along a typical geotherm (black), as well as changes with lateral temperature variations as depicted in (a). The green shaded region indicates the range of spin fractions, where the strongest effects on physical properties are expected (see also Figure 3).

depth interval over which ferropericlase properties will be mostly affected. Notably, ferropericlase will remain in the most impacted range of low-spin fraction in hot regions of the lower mantle up to the core-mantle boundary. Instead, the signature of the spin crossover will fade below about 1,800 km depth in cold mantle regions. Along a typical average geotherm, ferropericlase will not reach low-spin state. The low-spin fraction will reach a maximum of about 0.8 at ~2,600 km depth, before decreasing to about 0.6 at the core-mantle boundary. We note here that our calculation of the low-spin fraction does not include the difference in the vibrational free energy of different magnetic states. Including this component has previously been shown to increase the depth of the onset of the spin crossover at lower mantle temperatures (Wentzcovitch et al., 2009), which would strengthen our finding of a predominantly mixed-spin lowermost mantle.

Our calculated spin crossover range is broader than that predicted by previous computational results (Wu et al., 2013; Wu & Wentzcovitch, 2014) that have been used in the most recent attempt to compare the predicted seismic signature of the iron spin crossover to seismic tomography models (Shephard et al., 2021). A central observation of Shephard et al. (2021), discussed also by Cammarano et al. (2010), was that the P-velocity profile calculated for a pyrolytic mantle composition deviates substantially from the seismic Preliminary Reference Earth Model PREM below about 1,600 km. A broader spin crossover as predicted here will lead to a more smeared out effect of the compressional wave velocity softening, which might decrease the discrepancy between predictions and seismic models.

Based on our findings, significant lateral variations of mantle properties can be expected between regions of mixed-spin ferropericlase and regions of (close to) low-spin ferropericlase at depths below about 1,800 km. The reflection of these iso-depth property changes in ferropericlase in geophysical properties will depend on the property. The unique seismic signature of the spin crossover - most importantly the elevated  $V_S/V_P$  ratio (Marquardt et al., 2009; Shephard et al., 2021; Wu & Wentzcovitch, 2014) - is expected to affect seismic observables in all regions of the mantle where ferropericlase is in mixed-spin state, particularly the green shaded region in Figure 4b. However, transport properties, such as viscosity (Deng & Lee, 2017; Marquardt & Miyagi, 2015; Saha et al., 2013; Wentzcovitch et al., 2009), or electrical conductivity (Lin et al., 2013), will only be strongly affected if an interconnected network of ferropericlase develops, possibly as a result of mantle flow processes (Deng & Lee, 2017; Girard et al., 2016; Marquardt & Miyagi, 2015; Thielmann et al., 2020; Yamazaki et al., 2009).

#### 4. Conclusions

By combining novel time-resolved high-pressure XRD measurements with ab-initio computations, we show that the iron spin crossover leads to a broad, asymmetric softening of the bulk modulus with pressure. The broadness and shape of the elastic softening is sensitive to the distribution of iron atoms within the crystal lattice. Full

low-spin ferroperricite does not occur within the pressure-temperature-space explored here, which is representative for the lower mantle. This is in contrast to previous works that predict low-spin ferroperricite to dominate the lowermost mantle at all explored temperatures (Shephard et al., 2021). Based on our model, ferroperricite is in mixed-spin state throughout the lower mantle at all depths below about 1,000 km, including at the core-mantle boundary.

## Data Availability Statement

Data are available at <https://doi.org/10.6084/m9.figshare.20501790>.

## Acknowledgments

This research was supported through the DFG Research Unit FOR 2440 (grant MA4534/5-1) as well the European Union's Horizon 2020 research and innovation Programme (ERC grant 864877). HM thanks Paula Koelemeijer for discussions. The authors like to thank M. Wendt for providing technical assistance. The authors acknowledge DESY (Hamburg, Germany), a member of the Helmholtz Association HGF, for the provision of experimental facilities. The research leading to this result has been supported by the project CALIPSOplus under the Grant Agreement 730872 from the EU Framework Program for Research and Innovation HORIZON 2020. The first-principles calculations were performed on ARC3 and ARC4 part of the High-Performance Computing facilities at the University of Leeds, UK.

## References

- Anisimov, V. I., Aryasetiawan, F., & Lichtenstein, A. I. (1997). First-principles calculations of the electronic structure and spectra of strongly correlated systems: The LDA+U method. *Journal of Physics: Condensed Matter*, 9(4), 767–808. <https://doi.org/10.1088/0953-8984/9/4/002>
- Anisimov, V. I., Zaanen, J., & Andersen, O. K. (1991). Band theory and Mott insulators: Hubbard U instead of Stoner I. *Physical Review B*, 44(3), 943–954. <https://doi.org/10.1103/physrevb.44.943>
- Badro, J., Fiquet, G., Guyot, F., Rueff, J.-P., Struzhkin, V. V., Vanko, G., & Monaco, G. (2003). Iron partitioning in Earth's mantle: Toward a deep lower mantle discontinuity. *Science*, 300(5620), 789–791. <https://doi.org/10.1126/science.1081311>
- Birch, F. (1947). Finite elastic strain of Cubic crystals. *Physical Review*, 71(11), 809–824. <https://doi.org/10.1103/physrev.71.809>
- Blöchl, P. E. (1994). Projector augmented-wave method. *Physical Review B*, 50(24), 17953–17979.
- Cammarano, F., Marquardt, H., Speziale, S., & Tackley, P. J. (2010). Role of iron-spin transition in ferroperricite on seismic interpretation: A broad thermochemical transition in the mid mantle? *Geophysical Research Letters*, 37, L03308. <https://doi.org/10.1029/2009gl014583>
- Crowhurst, J. C., Brown, J. M., Goncharov, A. F., & Jacobsen, S. D. (2008). Elasticity of (Mg,Fe)O through the spin transition of iron in the lower mantle. *Science*, 319(5862), 451–453. <https://doi.org/10.1126/science.1149606>
- Davies, D. R., Goes, S., Davies, J. H., Schuberth, B. S. A., Bunge, H. P., & Ritsema, J. (2012). Reconciling dynamic and seismic models of Earth's lower mantle: The dominant role of thermal heterogeneity. *Earth and Planetary Science Letters*, 353–354, 253–269. <https://doi.org/10.1016/j.epsl.2012.08.016>
- Deng, J., & Lee, K. K. M. (2017). Viscosity jump in the lower mantle inferred from melting curves of ferroperricite. *Nature Communications*, 8(1). <https://doi.org/10.1038/s41467-017-02263-z>
- Dorfman, S. M., Prakapenka, V. B., Meng, Y., & Duffy, T. S. (2012). Intercomparison of pressure standards (Au, Pt, Mo, MgO, NaCl and Ne) to 2.5 Mbar. *Journal of Geophysical Research: Solid Earth*, 117(B8), B08210. <https://doi.org/10.1029/2012jb009292>
- Dudarev, S. L., Botton, G. A., Savrasov, S. Y., Humphreys, C. J., & Sutton, A. P. (1998). Electron-energy-loss spectra and the structural stability of nickel oxide: An LSDA+U study. *Physical Review B*, 57(3), 1505–1509. <https://doi.org/10.1103/physrevb.57.1505>
- Evans, W. J., Yoo, C.-S., Lee, G. W., Cynn, H., Lipp, M. J., & Visbeck, K. (2007). Dynamic diamond anvil cell (dDAC): A novel device for studying the dynamic-pressure properties of materials. *Review of Scientific Instruments*, 78(7), 073904–073906. <https://doi.org/10.1063/1.2751409>
- Fei, Y., Ricolleau, A., Frank, M., Mibe, K., Shen, G., & Prakapenka, V. (2007a). High-Pressure Geoscience Special Feature: Toward an internally consistent pressure scale. *Proceedings of the National Academy of Sciences*, 104(22), 9182–9186. <https://doi.org/10.1073/pnas.0609013104>
- Fei, Y., Zhang, L., Corgne, A., Watson, H., Ricolleau, A., Meng, Y., & Prakapenka, V. (2007b). Spin transition and equations of state of (Mg,Fe)O solid solutions. *Geophysical Research Letters*, 34, L17307. <https://doi.org/10.1029/2007gl030712>
- Girard, J., Amulele, G., Farla, R., Mohiuddin, A., & Karato, S.-I. (2016). Shear deformation of bridgmanite and magnesio-wüstite aggregates at lower mantle conditions. *Science*, 351(6269), 144–147. <https://doi.org/10.1126/science.1243113>
- Glazyrin, K., Khandarkhaeva, S., Dubrovinsky, L., & Sprung, M. (2020). Revisiting spin-state crossover in (Mg,Fe)O by means of high-resolution x-ray diffraction from a single crystal. *Physical Review B*, 101(18), 184203. <https://doi.org/10.1103/physrevb.101.184203>
- Glazyrin, K., Sinmyo, R., Bykova, E., Bykov, M., Cerantola, V., Longo, M., et al. (2017). Critical behavior of  $\text{Mg}_{1-x}\text{Fe}_x\text{O}$  at the pressure-induced iron spin-state crossover. *Physical Review B*, 95(21), 214412. <https://doi.org/10.1103/physrevb.95.214412>
- Holmström, E., & Stixrude, L. (2015). Spin crossover in ferroperricite from first-principles molecular dynamics. *Physical Review Letters*, 114(11), 117202.
- Humphrey, W., Dalke, A., & Schulten, K. (1996). VMD: Visual molecular dynamics. *Journal of Molecular Graphics*, 14(1), 33–38. [https://doi.org/10.1016/0263-7855\(96\)00018-5](https://doi.org/10.1016/0263-7855(96)00018-5)
- Irfune, T., Tsuchiya, T., & Schubert, G. (2015). 2.03 - Phase transitions and Mineralogy of the lower mantle. In *Treatise on Geophysics* (Second Edition, pp. 33–60). Elsevier. <https://doi.org/10.1016/b978-0-444-53802-4.00030-0>
- Jenei, Z., Liermann, H. P., Husband, R., Méndez, A. S. J., Pennicard, D., Marquardt, H., et al. (2019). New dynamic diamond anvil cells for tera-pascal per second fast compression x-ray diffraction experiments. *Review of Scientific Instruments*, 90(6), 065114. <https://doi.org/10.1063/1.5098993>
- Kantor, I., Dubrovinsky, L., McCammon, C., Steinle-Neumann, G., Kantor, A., Skorodumova, N., et al. (2009). Short-range order and Fe clustering in  $\text{Mg}_{1-x}\text{Fe}_x\text{O}$  under high pressure. *Physical Review B*, 80(1), 014204. <https://doi.org/10.1103/physrevb.80.014204>
- Karki, B. B., Wentzcovitch, R. M., Gironcoli, S., & Baroni, S. (1999). First-principles determination of elastic anisotropy and wave velocities of MgO at lower mantle conditions. *Science*, 286(5445), 1705–1707. <https://doi.org/10.1126/science.286.5445.1705>
- Kennett, B. L. N. (2021). The relative behaviour of bulk and shear modulus as an indicator of the iron spin transition in the lower mantle. *Earth and Planetary Science Letters*, 559, 116808. <https://doi.org/10.1016/j.epsl.2021.116808>
- Kresse, G., & Furthmüller, J. (1996). Efficiency of ab-initio total energy calculations for metals and semiconductors using a plane-wave basis set. *Computational Materials Science*, 6(1), 15–50. [https://doi.org/10.1016/0927-0256\(96\)00008-0](https://doi.org/10.1016/0927-0256(96)00008-0)
- Kresse, G., & Furthmüller, J. (1996). Efficient iterative schemes for ab initio total-energy calculations using a plane-wave basis set. *Physical Review B*, 54(16), 11169–11186. <https://doi.org/10.1103/physrevb.54.11169>
- Kresse, G., & Joubert, D. (1999). From ultrasoft pseudopotentials to the projector augmented-wave method. *Physical Review B*, 59(3), 1758–1775. <https://doi.org/10.1103/physrevb.59.1758>

- Liermann, H.-P., Konopkova, Z., Morgenroth, W., Glazyrin, K., Bednarcik, J., McBride, E. E., et al. (2015). The Extreme conditions Beam-line P02.2 and the Extreme conditions Science Infrastructure at PETRA III. *Journal of Synchrotron Radiation*, 22(4), 908–924. <https://doi.org/10.1107/s1600577515005937>
- Lin, J.-F., Speziale, S., Mao, Z., & Marquardt, H. (2013). Effects of the electronic spin transitions of iron in lower-mantle minerals: Implications to deep-mantle geophysics and geochemistry. *Reviews of Geophysics*, 51(2), 244–275. <https://doi.org/10.1002/rog.20010>
- Lin, J.-F., Struzhkin, V. V., Jacobsen, S. D., Hu, M. Y., Chow, P., Kung, J., et al. (2005). Spin transition of iron in magnesiowüstite in the Earth's lower mantle. *Nature*, 436(7049), 377–380. <https://doi.org/10.1038/nature03825>
- Lyubutin, I. S., Struzhkin, V. V., Mironovich, A. A., Gavriluk, A. G., Naumov, P. G., Lin, J.-F., et al. (2013). Quantum critical point and spin fluctuations in lower-mantle ferroperricite. *Proceedings of the National Academy of Sciences*, 110(18), 7142–7147. <https://doi.org/10.1073/pnas.1304827110>
- Mao, Z., Lin, J.-F., Liu, J., & Prakapenka, V. B. (2011). Thermal equation of state of lower-mantle ferroperricite across the spin crossover. *Geophysical Research Letters*, 38(23), L23308. <https://doi.org/10.1029/2011gl049915>
- Marquardt, H., Buchen, J., Mendez, A. S. J., Kurnosov, A., Wendt, M., Rothkirch, A., et al. (2018). Elastic softening of (Mg<sub>0.8</sub>Fe<sub>0.2</sub>)O ferroperricite across the iron spin crossover measured at seismic frequencies. *Geophysical Research Letters*, 45(14), 6862–6868. <https://doi.org/10.1029/2018gl077982>
- Marquardt, H., & Miyagi, L. (2015). Slab stagnation in the shallow lower mantle linked to an increase in mantle viscosity. *Nature Geoscience*, 8(4), 311–314. <https://doi.org/10.1038/ngeo2393>
- Marquardt, H., Speziale, S., Reichmann, H. J., Frost, D. J., & Schilling, F. R. (2009). Single-crystal elasticity of (Mg<sub>0.9</sub>Fe<sub>0.1</sub>)O to 81 GPa. *Earth and Planetary Science Letters*, 287(3–4), 345–352. <https://doi.org/10.1016/j.epsl.2009.08.017>
- Méndez, A. S. J., Marquardt, H., Husband, R., Schwark, I., Mainberger, J., Glazyrin, K., et al. (2020). A resistively-heated dynamic diamond anvil cell (RHdDAC) for fast compression x-ray diffraction experiments at high temperatures. *Review of Scientific Instruments*, 91. <https://doi.org/10.1063/5.0007557>
- Méndez, A. S. J., Trybel, F., Husband, R. J., Steinle-Neumann, G., Liermann, H. P., & Marquardt, H. (2021). Bulk modulus of H<sub>2</sub>O across the ice VII – ice X transition measured by time-resolved x-ray diffraction in dynamic diamond anvil cell experiments. *Physical Review B*, 103(6), 064104.
- Meng, Y., Weidner, D. J., & Fei, Y. (1993). Deviatoric stress in a quasi-hydrostatic diamond anvil cell: Effect on the volume-based pressure calibration. *Geophysical Research Letters*, 20(12), 1147–1150. <https://doi.org/10.1029/93gl01400>
- Monkhorst, H. J., & Pack, J. D. (1976). Special points for Brillouin-zone integrations. *Physical Review B*, 13(12), 5188–5192. <https://doi.org/10.1103/physrevb.13.5188>
- Muir, J. M. R., & Brodholt, J. P. (2015). Elastic properties of ferroperricite at lower mantle conditions and its relevance to ULVZs. *Earth and Planetary Science Letters*, 417, 40–48. <https://doi.org/10.1016/j.epsl.2015.02.023>
- Murnaghan, F. D. (1944). The compressibility of Media under Extreme pressures. *Proceedings of the National Academy of Sciences*, 30(9), 244–247. <https://doi.org/10.1073/pnas.30.9.244>
- Oganov, A. R., Brodholt, J. P., & Price, G. D. (2001). Ab initio elasticity and thermal equation of state of MgSiO<sub>3</sub> perovskite. *Earth and Planetary Science Letters*, 184(3), 555–560. [https://doi.org/10.1016/s0012-821x\(00\)00363-0](https://doi.org/10.1016/s0012-821x(00)00363-0)
- Pennicard, D., Lange, S., Smoljanin, S., Hirsemann, H., Graafsma, H., Epple, M., et al. (2013). The LAMBDA photon-counting pixel detector. *Journal of Physics: Conference Series*, 425(6), 062010. <https://doi.org/10.1088/1742-6596/425/6/062010>
- Pennicard, D., Smoljanin, S., Pithan, F., Sarajlic, M., Rothkirch, A., Yu, Y., et al. (2018). LAMBDA 2M GaAs—A multi-megapixel hard X-ray detector for synchrotrons. *Journal of Instrumentation*, 13(01), C01026. <https://doi.org/10.1088/1748-0221/13/01/c01026>
- Perdew, J. P., & Zunger, A. (1981). Self-interaction correction to density-functional approximations for many-electron systems. *Physical Review B*, 23(10), 5048–5079. <https://doi.org/10.1103/physrevb.23.5048>
- Prescher, C., & Prakapenka, V. B. (2015). DIOPTAS: A program for reduction of two-dimensional X-ray diffraction data and data exploration. *High Pressure Research*, 35(3), 223–230. <https://doi.org/10.1080/08957959.2015.1059835>
- Saha, S., Bengtson, A., & Morgan, D. (2013). Effect of anomalous compressibility on Fe diffusion in ferroperricite throughout the spin crossover in the lower mantle. *Earth and Planetary Science Letters*, 362(0), 1–5. <https://doi.org/10.1016/j.epsl.2012.11.032>
- Shannon, R. (1976). Revised effective ionic radii and systematic studies of interatomic distances in halides and chalcogenides. *Acta Crystallographica Section A*, 32(5), 751–767. <https://doi.org/10.1107/s0567739476001551>
- Shephard, G. E., Houser, C., Hernlund, J. W., Valencia-Cardona, J. J., Trønnes, R. G., & Wentzcovitch, R. M. (2021). Seismological expression of the iron spin crossover in ferroperricite in the Earth's lower mantle. *Nature Communications*, 12(1), 5905. <https://doi.org/10.1038/s41467-021-26115-z>
- Solomatova, N., Jackson, J., Stührhahn, W., Wicks, J., Zhao, J., Toellner, T. S., et al. (2016). Equation of state and spin crossover of (Mg,Fe)O at high pressure, with implications for explaining topographic relief at the core-mantle boundary. *American Mineralogist*, 101(5), 1084–1093. <https://doi.org/10.2138/am-2016-5510>
- Speziale, S., Lee, V. E., Clark, S. M., Lin, J. F., Pasternak, M. P., & Jeanloz, R. (2007). Effects of Fe spin transition on the elasticity of (Mg,Fe)O magnesiowüstite and implications for the seismological properties of the Earth's lower mantle. *Journal of Geophysical Research*, 112. <https://doi.org/10.1029/2006jb004730>
- Speziale, S., Milner, A., Lee, V. E., Clark, S. M., Pasternak, M. P., & Jeanloz, R. (2005). Iron spin transition in Earth's mantle. *Proceedings of the National Academy of Sciences*, 102(50), 17918–17922. <https://doi.org/10.1073/pnas.0508919102>
- Thielmann, M., Golabek, G. J., & Marquardt, H. (2020). Ferroperricite control of lower mantle rheology: Impact of Phase Morphology. *Geochemistry, Geophysics, Geosystems*, 21(2), e2019GC008688. <https://doi.org/10.1029/2019gc008688>
- Tsuchiya, T., Wentzcovitch, R. M., Silva, C. R. S., & Gironcoli, S. (2006). Spin transition in magnesiowüstite in Earth's lower mantle. *Physical Review Letters*, 96(19), 198501–198504. <https://doi.org/10.1103/physrevlett.96.198501>
- Waychunas, G. A., Dollase, W. A., & Ross, C. R. (1994). Short-range order measurements in MgO-FeO and MgO-LiFeO<sub>2</sub> solid solutions by DLS simulation-assisted EXAFS analysis. *American Mineralogist*, 79(3–4), 274–288.
- Wentzcovitch, R. M., Justo, J. F., Wu, Z., Silva, C. R. S., Yuen, D. A., & Kohlstedt, D. (2009). Anomalous compressibility of ferroperricite throughout the iron spin cross-over. *Proceedings of the National Academy of Sciences*, 106(21), 8447–8452. <https://doi.org/10.1073/pnas.0812150106>
- Wu, Z., Justo, J. F., & Wentzcovitch, R. M. (2013). Elastic anomalies in a spin-crossover system: Ferroperricite at lower mantle conditions. *Physical Review Letters*, 110(22), 228501. <https://doi.org/10.1103/physrevlett.110.228501>
- Wu, Z., & Wentzcovitch, R. M. (2014). Spin crossover in ferroperricite and velocity heterogeneities in the lower mantle. *Proceedings of the National Academy of Sciences*, 111, 10468–10472. <https://doi.org/10.1073/pnas.1322427111>

- Yamazaki, D., Yoshino, T., Matsuzaki, T., Katsura, T., & Yoneda, A. (2009). Texture of (Mg,Fe)SiO<sub>3</sub> perovskite and ferro-periclasite aggregate: Implications for rheology of the lower mantle. *Physics of the Earth and Planetary Interiors*, 174(1–4), 138–144. <https://doi.org/10.1016/j.pepi.2008.11.002>
- Yang, J., Tong, X., Lin, J.-F., Okuchi, T., & Tomioka, N. (2015). Elasticity of ferropericlasite across the spin crossover in the Earth's lower mantle. *Scientific Reports*, 5, 17188. <https://doi.org/10.1038/srep17188>